An all-fiber Fabry-Perot sensor for wide-range static and dynamic pressure measurement

LEXING XUE[1,2,*], WEN PAN[1], ZIHAO GAO[2], RUIXIANG CHEN[2], HAIBIN CHEN[2,3]
[1]*Xi'an Modern Chemistry Research Institute, Xi'an 710065, China*
[2]*School of Optoelectronic Engineering, Xi'an Technological University, Xi'an 710021, China*
[3]*National Key Laboratory of Energetic Materials, Xi'an 710065, China*

To address the demands for high-precision and wide-range pressure measurement, an all-fiber diaphragm-type Fabry-Perot pressure sensor was designed. Based on principles and simulation experiments, static pressure calibration and dynamic pressure measurement systems were set up to evaluate the sensing performance. Experimental results exhibit a wavelength sensitivity of 96.4 pm/MPa and a cavity length sensitivity of 5.14 nm/MPa in static pressure range of 0 ~ 60 MPa. In dynamic pressure measurements, shock wave signals were captured with a measured pressure peak of 4.02 MPa and a rise time of 114 ns. The sensor is suitable for high-temperature oil monitoring and others.

(Received August 5, 2025; accepted April 6, 2026)

Keywords: Fabry-Perot interferometer, Fiber-optic sensor, Pressure measurement

1. Introduction

With the rapid advancement of aerospace, chemical metallurgy, petroleum, and power industries, there is a growing demand for real-time monitoring of pressure parameters in harsh environments [1-4]. In the field of pressure measurement, fiber-optic sensors have demonstrated significant potential compared to traditional electrical sensors due to their notable advantages, including robustness in harsh environments, immunity to electromagnetic interference, and compact size [5-7]. The main configurations of fiber-optic pressure sensors include Fiber Bragg Grating (FBG) [8,9], Long Period Fiber Grating (LPFG) [10], Fabry-Perot interferometer (FPI) [11], Mach-Zehnder interferometer (MZI) [12], and other interferometric structures. Among these, the FPI has been extensively utilized for pressure measurement applications due to its simple structure, high stability, rapid response, and exceptional accuracy. Its applications extend across various fields, such as medical monitoring, structural health assessment, and high-pressure oil well monitoring [13-15].

Common fabrication techniques for fiber-optic Fabry-Perot (F-P) pressure sensors encompass femtosecond laser (fs) processing, MEMS (Micro-Electro-Mechanical Systems), magnetron sputtering, and chemical vapor deposition [16-19]. In 2013, Y. Zhang et al. [20] presented an fs micromachining method to fabricate fiber-optic F-P pressure sensors for high-temperature pressure measurement. The sensor exhibits a maximum pressure measurement range of 0.69 MPa and a sensitivity of 0.28 μm/MPa. However, this method is constrained by a limited pressure measurement range, high equipment costs, and complex parameter tuning. In 2020, W. Ma et al. [21] proposed a high-finesse, optical-fiber, extrinsic FPI (EFPI) pressure sensor based on a MEMS technique. The sensor exhibited a pressure measurement range of 0 ~ 1 MPa and a cavity length sensitivity of 1.598 μm/MPa. Although MEMS technology enables the fabrication of highly sensitive sensors, it is primarily focused on small-range pressure measurements and involves complex manufacturing processes with relatively high costs. In 2022, Y. Wang et al. [22] proposed an F-P sensor with vacuum sputter deposited carbon coating films. The sensitivity and accuracy of the F-P sensor incorporating carbon film deposition were determined to be 0.369 μm/MPa and 0.02% of full scale (FS), respectively, across a pressure measurement range of 0 ~ 42 MPa. Nevertheless, this sensor faces challenges such as high manufacturing costs, low yield, and stringent material property requirements.

In recent years, extensive research has been conducted on high-sensitivity fiber-optic F-P pressure sensors, demonstrating notable advancements in their development and application. Nevertheless, these sensors frequently face several limitations, such as a restricted pressure measurement range, intricate fabrication procedures, elevated production costs, demanding material specifications, and inadequate long-term stability.

To address these challenges, an all-fiber F-P pressure sensor is proposed in this study. The sensor is manufactured through a process involving fusion splicing, precision cutting, and chemical etching of standard single-mode fiber (SMF), hollow-core fiber (HCF), and multi-mode fiber (MMF). The proposed sensor demonstrates several significant advantages, including a compact design, cost effectiveness, straightforward fabrication, excellent stability, and an extended pressure measurement range. These characteristics render it particularly well-suited for real-time online monitoring of pressure parameters under harsh environmental conditions.

2. Principles and design

2.1. Sensor structure

The structural diagram of the fiber-optic F-P pressure sensor is illustrated in Fig. 1. The F-P cavity is fabricated by splicing a segment of HCF between a segment of SMF and a piece of MMF., with the length of the HCF determining the cavity length of the F-P structure. The MMF is utilized as the pressure-sensitive diaphragm, and its length corresponds to the thickness of the diaphragm. Owing to the substantially smaller numerical aperture of the SMF relative to that of the HCF, the scattering angle of light entering the cavity from the SMF core is diminished, resulting in reduced scattering losses within the cavity. Furthermore, the HCF is employed as the F-P cavity, and its high mechanical strength ensures that deformation is significantly reduced during the fusion splicing process. Consequently, a more regular and symmetrical cavity geometry is formed, resulting in enhanced collimation of the optical path.

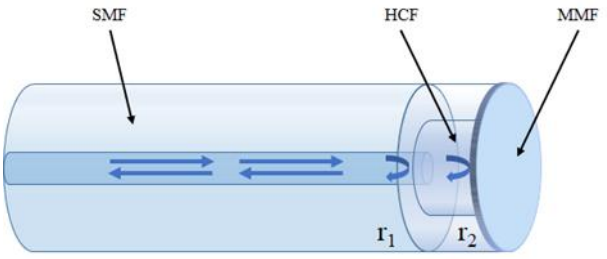

Fig. 1. Schematic diagram of fiber-optic F-P pressure sensor structure (colour online)

2.2. Sensing principle of sensor

As illustrated in Fig. 1, light is transmitted through the SMF.

When it reaches the interface between the SMF and the HCF, which functions as the first reflective surface r_1, a portion of the light is reflected, whereas the remainder propagates further. When the transmitted light reaches the interface between the HCF and the MMF, it is reflected at the second reflective surface r_2. The light reflected from r_2 interferes with that reflected from r_1, resulting in the generation of an interference spectrum at r_1. Since the reflectivity at the fiber end face is less than 5%, the multiple-beam interference can be approximated by a two-beam interference model [23], allowing the F-P cavity to be treated as a two-beam interference system. Based on the spectral reflectance model of a single F-P cavity [24], the following expression is derived:

$$R_{\lambda,d} = \frac{R_1 + R_2 - 2\sqrt{R_1 R_2}\cos\varphi}{1 + R_1 R_2 - 2\sqrt{R_1 R_2}\cos\varphi}, \tag{1}$$

$$\Delta = 2nL, \tag{2}$$

$$\varphi = \frac{2\pi}{\lambda}\Delta = \frac{4\pi}{\lambda}nL, \tag{3}$$

here, $R_{\lambda,d}$ represents the reflectivity of the sensor, where R_1 and R_2 denote the reflectivity of the first and second reflective surfaces, respectively. L represents the length of the F-P cavity, Δ represents the optical path difference between two adjacent reflected beams, denotes the refractive index of the air cavity, φ represents the phase difference induced by the optical path difference, and λ denotes the wavelength of light.

According to the above formulation, when pressure is applied to the sensor, the length of the F-P cavity is reduced, resulting in a phase shift in the reflected spectrum. Through analysis of the phase difference in the reflected spectrum, the cavity length of the sensor under a specific pressure can be precisely determined.

2.3. Simulation of sensors

To determine the diaphragm parameters, mechanical analysis of the fiber-optic F-P pressure sensor was performed using finite element simulation software, and the pressure-sensitive diaphragm parameters were calculated based on theoretical formulas. The simulation procedure was conducted as follows: 1) The sensor model was built, and the material properties were defined; 2) The physical field parameters were adjusted, and the corresponding boundary conditions were applied; 3) The model was discretized through meshing; 4) Simulation computations were performed.

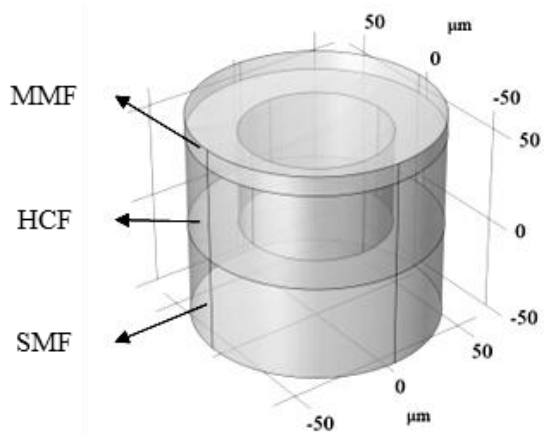

Fig. 2. Three-dimensional diagram of all fiber F-P structure in simulation software

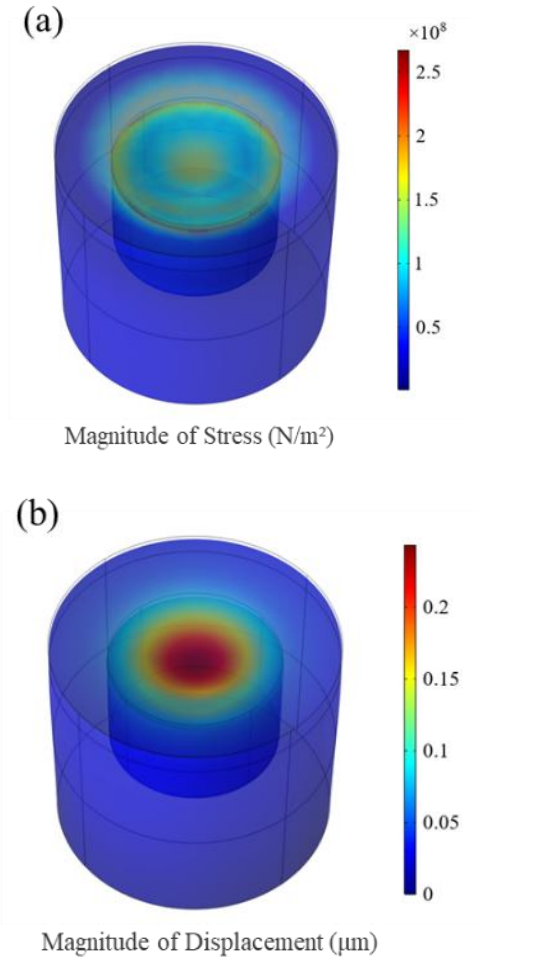

Fig. 3. (a) Sensor pressure deformation distribution. (b) Sensor compressive stress distribution (colour online)

The fiber-optic F-P pressure sensor was modeled using the structural mechanics module of the simulation software, and its three-dimensional structure is depicted in Fig 2. The SMF was designed to have a length of 60 μm and a diameter of 125 μm. The HCF was constructed by subtracting two concentric cylinders of different diameters, yielding a hollow-core region with a diameter of 75 μm, a length of 60 μm, and an outer diameter matching that of the SMF. The pressure-sensitive diaphragm was designed with a thickness ranging from 8 to 20 μm and an outer diameter equal to that of the SMF. These three components were combined into a single entity for the simulation.

Boundary loads were applied to the sensor model, and fixed constraints were imposed on the bottom surface to ensure computational stability. The deformation distribution of the diaphragm under applied pressure is shown in Fig 3(a), and the stress distribution of the sensor under pressure is depicted in Fig 3(b).

The boundary pressure load and diaphragm thickness were systematically adjusted to investigate their impact on the sensor's performance. The boundary pressure load was set to range from 0 MPa to 60 MPa in increments of 5 MPa, and the diaphragm thickness was varied from 8 μm to 20 μm in increments of 1 μm. Structural-mechanical and characteristic frequency simulations were performed on the sensor model to determine the deformation of the F-P cavity under applied pressure and the characteristic frequencies at different diaphragm thicknesses. As shown in Fig. 4, the simulation results demonstrate that the slope of the displacement curve decreases with increasing diaphragm thickness, indicating a reduction in the cavity length sensitivity of the F-P cavity. Meanwhile, the characteristic frequency decreases as the diaphragm thickness are reduced. Therefore, by comprehensively considering sensitivity, characteristic frequency, and mechanical strength, we selected a diaphragm thickness of 14 μm to ensure optimal performance for both static and dynamic pressure measurements.

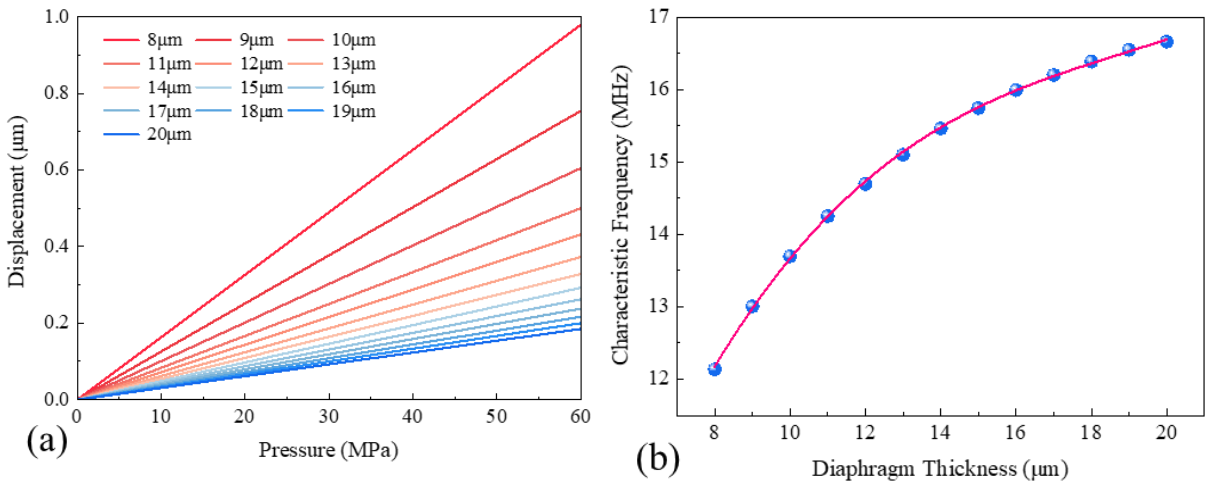

Fig. 4. (a) Pressurized deformation of sensor F-P cavity with different diaphragm thicknesses (b) Characteristic frequencies of diaphragms with different thicknesses (colour online)

2.4. Fabrication of sensors

Based on the simulation results, a fiber-optic F-P pressure sensor was fabricated, incorporating a HCF with a length of 60 μm and a pressure-sensitive diaphragm thickness of 14 μm The materials used for fabricating the sensor included: standard SMF (SMF-28e+, Corning) with an outer diameter of 125 μm; HCF (Polymicro capillary, Molex) with an inner diameter of 75 μm and an outer diameter of 125 μm; and MMF (Wuhan Taida Optoelectronics Technology) with a core diameter of 105 μm and an outer diameter of 125 μm, which was selected to achieve a more uniform etching profile and maintain the integrity of the diaphragm.

The fabrication process consisted of the following steps: 1) The coating of the SMF was removed, and a smooth end face was prepared, after which the SMF was fusion-spliced with the HCF; 2) The cutting tool was fixed under a microscope, and the HCF was cut to the appropriate cavity length using a precision translation stage; 3) The MMF was fusion-spliced to the end of the HCF, forming the F-P cavity; 4) The MMF was cut using a precision translation stage to obtain the pressure-sensitive diaphragm; 5) The diaphragm was optimized by etching with hydrofluoric acid (HF) to achieve thinning and anti-reflection effects.

It is noteworthy that, at room temperature, the etching rate of SiO_2 in a 49% HF solution is approximately 1 μm/min. The thickness of the diaphragm in this sensor structure is controlled by the etching duration. Prolonged etching duration may compromise the fusion joint between the HCF and the SMF, leading to a deterioration in the fiber's reflectivity and interference spectrum, as well as potential damage to the sensor probe. Consequently, precise control of the etching duration is essential. In the experiment, the diaphragm was fabricated from a germanium-doped core MMF with a core/cladding diameter of 105/125 μm. During the HF etching process, the etching rates of the core and cladding differ, with regions of higher doping concentration exhibiting faster etching. This results in the formation a concave front surface of the sensor diaphragm. Although the front surface is not flat, actually it can reduce unwanted reflections from this interface. Fig. 5 presents a series of electron microscope images documenting the entire etching process, along with a detailed record of the etching time and the corresponding thickness of the diaphragm at each interval. Here, for the fabrication of the FP diaphragm, an MMF is used instead of an SMF or a coreless fiber, because flatness of the diaphragm made from an MMF is much better than an SMF, but not too flat to introduce unwanted reflection interferences.

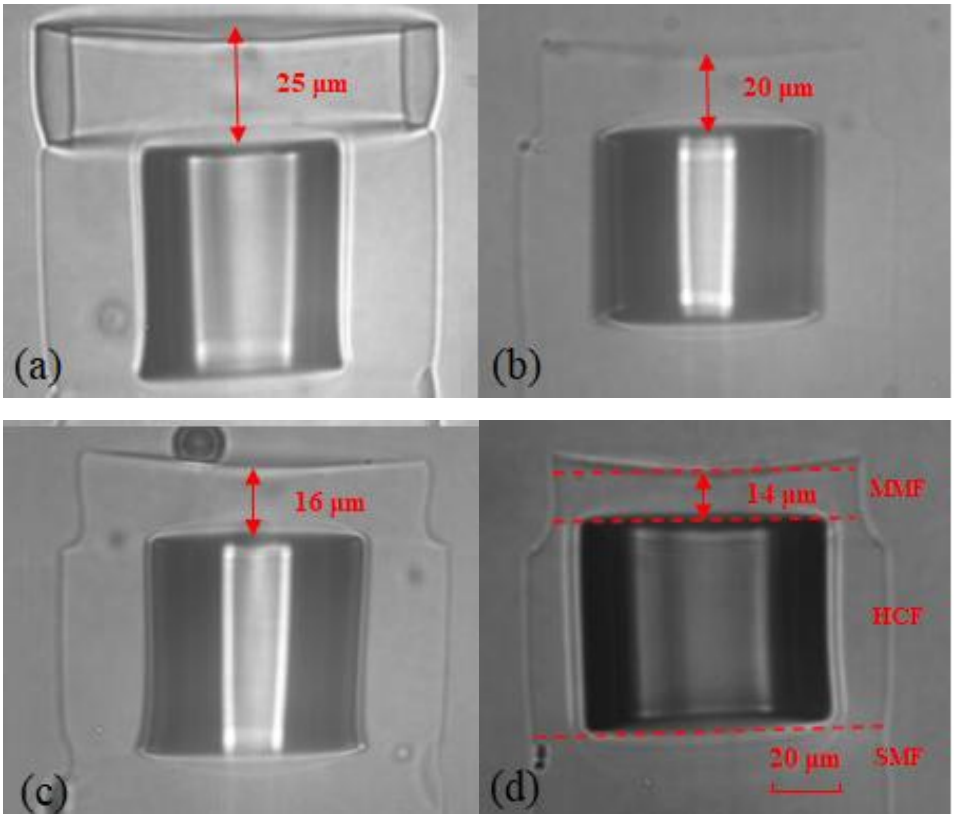

Fig. 5. (a) Initial state. (b) Etching for 5 minutes. (c) Additional etching for 5 minutes. (d) Final etching for 3 minutes and 10 seconds (colour online)

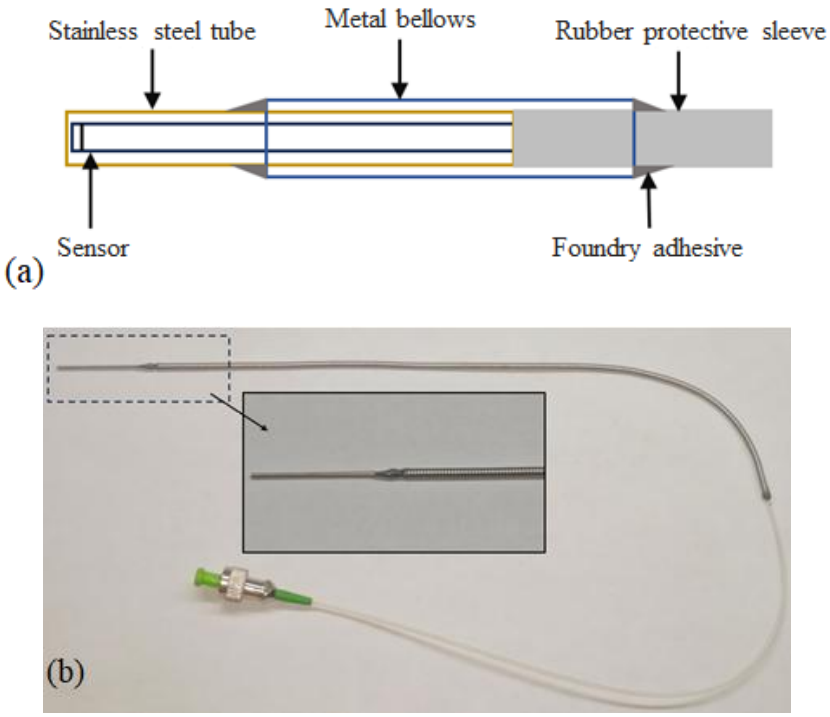

Fig. 6. (a) The sensor encapsulation structure. (b) Physical picture of sensor encapsulation (colour online)

From the etching results, it can be observed that after the first 5-minute etching, the diaphragm thickness decreased from 25 μm to 20 μm, a reduction of 5 μm. After the second 5-minute etching, the diaphragm

thickness further decreased from 20 μm to 16 μm, a reduction of 4 μm. Following the second etching, the diaphragm thickness approached the target value, prompting a reduction in etching time for the final step. The last etching step, lasting 3 minutes and 10 seconds, resulted in a diaphragm thickness of 14 μm, meeting the simulation requirement of 8-15 μm for the diaphragm thickness.

To reduce the impact of external factors on signal reception during experiments and to protect the sensor for improved environmental practicality, the sensor was encapsulated for pressure measurement experiments without compromising its sensitivity. The diagram of the sensor encapsulation structure is shown in Fig 6(a). The primary materials used for encapsulation are metal bellows and stainless-steel tubes. The stainless-steel tube serves as the front end of the encapsulation, while the metal bellows acts as the rear end, providing both flexibility and protective fixation. The encapsulated sensor is shown in Fig. 6(b).

3. Experimental setup and results

3.1. Static pressure measurement

The pressure calibration experimental setup is depicted in Fig. 7. The system consists of a superluminescent diode (SLD) broadband light source (Thorlabs, output wavelength range: 1440-1640 nm, 3 dB bandwidth: 90 nm, center wavelength: 1568 nm), an optical spectrum analyzer (OSA, MS9740A, Anritsu, Japan, spectral measurement range: 600-1750 nm, dynamic measurement range: ≥60 dB, maximum resolution: 0.03 nm), an optical fiber circulator, a fiber-optic F-P pressure sensor, and a desktop hydraulic pump (ConST135A, pressure range: 0–100 MPa).

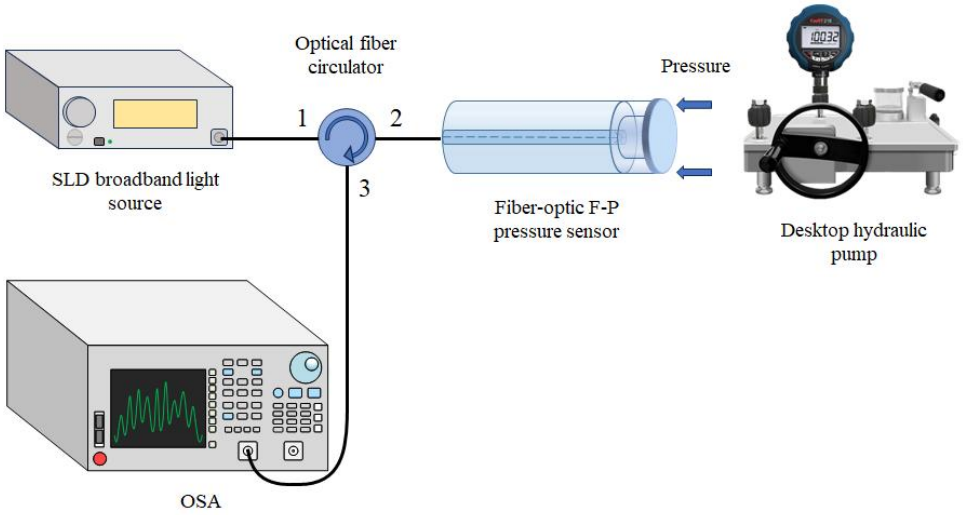

Fig. 7. Pressure measurement experimental system (colour online)

Light emitted from the SLD broadband source is directed into port 1 of the fiber optic circulator and then routed to port 2, where it is transmitted into the fiber-optic F-P pressure sensor. When pressure is applied, the interference spectrum, which carries information about the cavity length of the F-P cavity, is guided through port 3 of the circulator and received by the OSA. By analyzing the spectral information of the sensor from the OSA, the variation in the cavity length of the sensor can be determined.

The encapsulated sensor, with a pressure-sensitive diaphragm thickness of 14 μm, was placed in the hydraulic pump. Pressure was applied in increments of 5 MPa over a range of 0–60 MPa, and the corresponding spectra of the sensor at different pressures were recorded, as shown in Fig. 8. As shown in the figure, the reflection spectrum of the fiber-optic F-P pressure sensor exhibits a blue shift with increasing applied pressure.

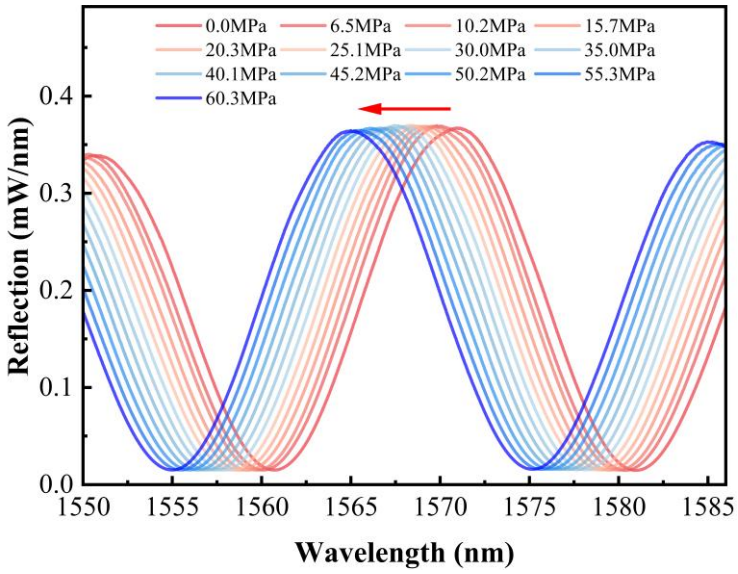

Fig. 8. Reflection spectra of fiber-optic F-P pressure sensor under different pressures (colour online)

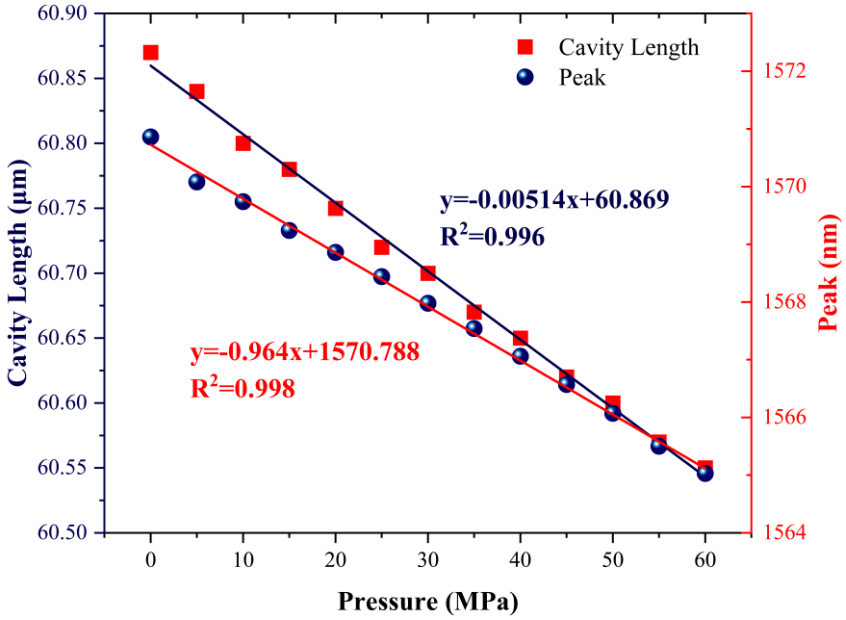

Fig. 9. Relationship between pressure and cavity length of fiber-optic F-P pressure sensor (colour online)

The cavity length of the sensor under corresponding pressures was determined by employing the cavity length matching method. Scatter plots of the cavity length values at different pressures and the corresponding peak values were generated and fitted linearly. The results are shown in Fig. 9.

As shown by the blue data points in Fig 9, the peak position of the sensor's reflection spectrum exhibited a blue shift of 5.83 nm as the pressure increased from 0 MPa to 60.35 MPa. A linear fit between the pressure and peak position yielded a wavelength sensitivity of 96.4 pm/MPa and a linearity of 0.998. Similarly, as indicated by the red data points in Fig. 9, the cavity length of the sensor decreased by 0.312 μm as the pressure increased from 0 MPa to 60.35 MPa. A linear fit between the cavity length and pressure revealed a sensitivity of 5.14 nm/MPa and a linearity of 0.996.

The static pressure measurement experiment demonstrates that the sensor can withstand pressures of up to 60 MPa. During the pressure loading experiment, as the pressure increased from 0 MPa to 60.35 MPa, the cavity length of the sensor decreased by 0.312 μm, and the reflection spectrum shifted by 5.83 nm. This corresponds to a cavity length reduction of 5.14 nm and a wavelength change of 96.4 pm for every 1 MPa increase in pressure.

According to the conversion formula between cavity length sensitivity and wavelength sensitivity:

$$S_\lambda = \frac{\lambda}{L} S_L. \tag{4}$$

By substituting the experimentally measured cavity length sensitivity of 5.14 nm/MPa, the wavelength of 1570.77 nm corresponding to the same interference order peak, and the cavity length of 60.87 μm into Equation (4), we obtain:

$$S_\lambda = \frac{\lambda}{L} S_L = \frac{1.57077}{60.87} \times 5.14 = 132.6\ pm/MPa \tag{5}$$

The experimentally measured wavelength sensitivity is 96.4 pm/MPa, which shows a certain discrepancy compared to the wavelength sensitivity of 132.6 pm/MPa derived from the above relationship. The primary reasons for this discrepancy include the following:

During the experiment, temperature fluctuations in the medium caused by pressurization and depressurization processes can introduce variations in wavelength measurements.

The cavity length is determined using the cross-correlation demodulation method, which introduces a certain level of measurement error, leading to inaccuracies in the cavity length sensitivity. Furthermore, errors in the peak-finding algorithm can cause uncertainties in the peak position, resulting in deviations in the wavelength sensitivity.

In the structural mechanics finite element simulation, the cavity length of the sensor with a diaphragm thickness of 14 μm decreased by 0.324 μm as the pressure increased from 0 MPa to 60 MPa. This corresponds to a cavity length reduction of 5.40 nm per 1 MPa increase in pressure. A comparison between the simulation and experimental results is shown in Fig. 10. For each MPa of pressure, the difference in cavity length reduction between the simulation and experimental results was 0.26 nm. As shown by the comparison, the experimental and simulation results exhibit a high degree of consistency.

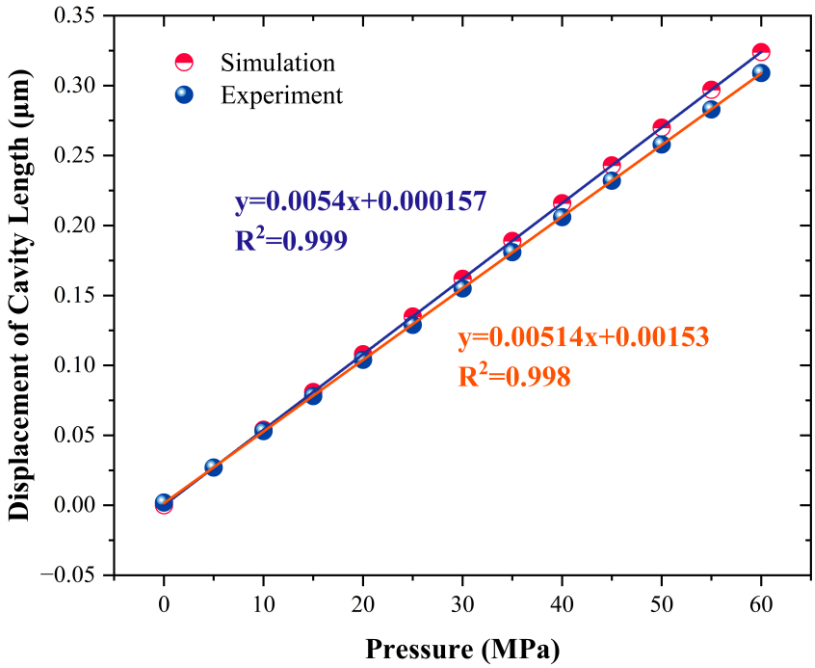

Fig. 10. Comparison between experimental and simulation results of cavity length variation under different pressures (colour online)

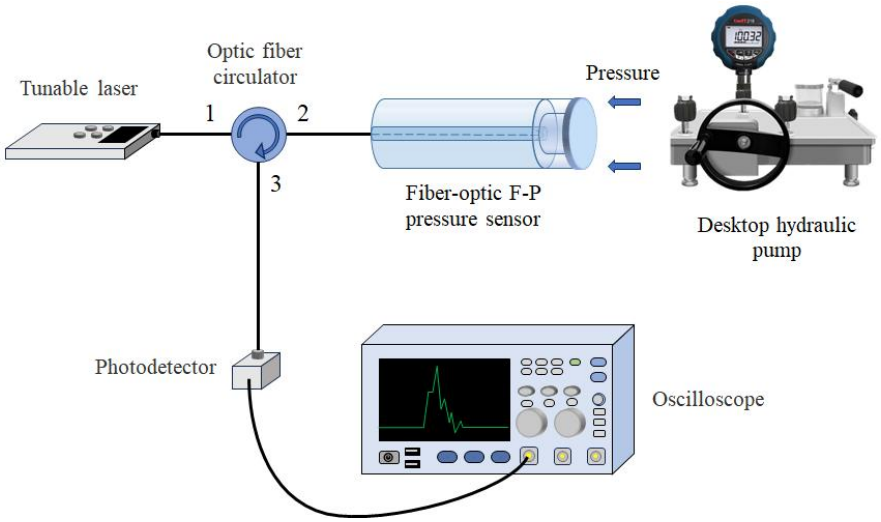

Fig. 11. Schematic diagram of static pressure measurement experiment system (colour online)

After completing the static pressure calibration test, a static pressure measurement experiment was performed. The schematic diagram of the measurement system is shown in Fig. 11. The system consists of a tunable laser (wavelength tunable range: 1529–1567 nm, maximum output power: 40 mW, tuning resolution: 1 pm, power stability: $< \pm 0.03$ dB/hr), a fiber optic circulator, a photodetector (wavelength response range: 800 ~ 1700 nm, rise time: 70 ps), an oscilloscope, a encapsulated fiber-optic F-P pressure sensor, and a benchtop hydraulic pump.

After setting up the static pressure measurement experimental system, the laser wavelength was adjusted to the linear region of the reflection spectrum based on the principle of intensity demodulation, and the quadrature operating point of the fiber-optic F-P pressure sensor was determined. As shown in Fig. 12, based on the reflection spectrum from the static pressure calibration experiment and the tuning range of the tunable laser (1529–1567 nm), the quadrature operating point of the fiber-optic F-P pressure sensor was selected as 1563.1 nm, and the operating wavelength of the tunable laser was set to 1563.1 nm.

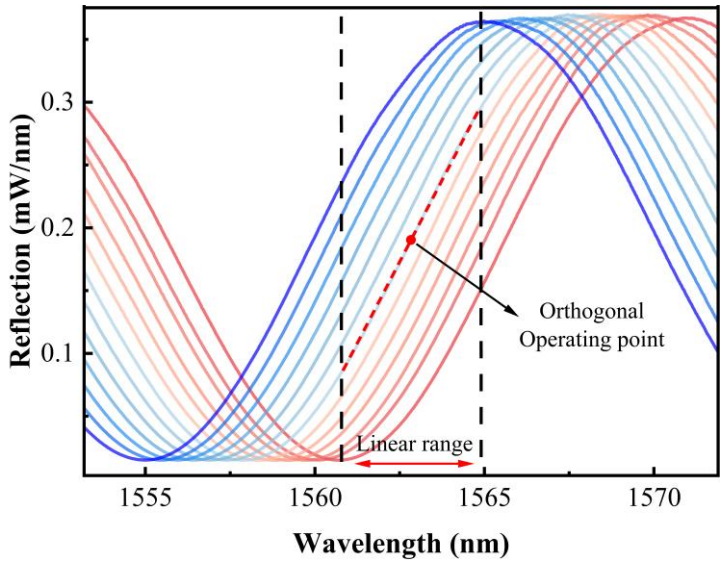

Fig. 12. Schematic diagram of linear intervals and orthogonal working points (colour online)

A benchtop hydraulic pump was used to apply and release pressure on the fiber-optic F-P pressure sensor over a range of 0 ~ 60 MPa in increments of 5 MPa. The voltage values displayed on the oscilloscope corresponding to each pressure level were recorded. The data were plotted to determine the voltage values during

both the pressurization and depressurization processes, as shown in Fig 13. During the pressurization process, the voltage increased from 11 mV to 607 mV as the pressure rose from 0 MPa to 60 MPa, resulting in a voltage change of 596 mV. A linear fit of the data points revealed a voltage sensitivity of 9.83 mV/MPa and a linearity of 0.998. During the depressurization process, the voltage decreased from 607 mV to 19 mV as the pressure dropped from 60 MPa to 0 MPa, corresponding to a voltage change of 588 mV, with a voltage sensitivity of 9.68 mV/MPa and a linearity of 0.998.

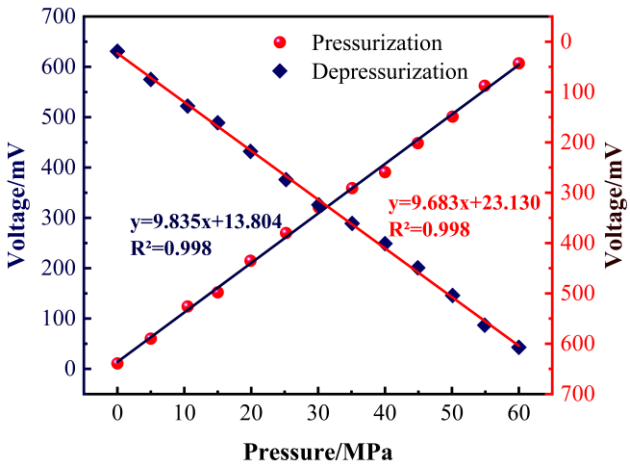

Fig. 13. Experimental results of static pressure measurement (colour online)

Based on the above data, the average voltage sensitivity of 9.86 mV/MPa, derived from the pressurization and depressurization processes, was used as the voltage sensitivity of the fiber-optic F-P pressure sensor.

3.2. Dynamic pressure measurement

Following the completion of the preliminary experiments, dynamic pressure measurements were performed using shock wave signals as the dynamic pressure source. The shock wave signals were generated by a lamp-pumped YAG laser through Q-switching to induce pulsed laser plasma [25]. When the laser was focused on the target material, ionization took place, resulting in a localized explosion that produced shock wave signals [26]. The schematic diagram of the dynamic pressure measurement experimental system is shown in Fig. 14. The system consists of a tunable laser, a fiber optic isolator, a custom photodetector, an oscilloscope, a encapsulated fiber-optic F-P pressure sensor, and a lamp-pumped YAG laser.

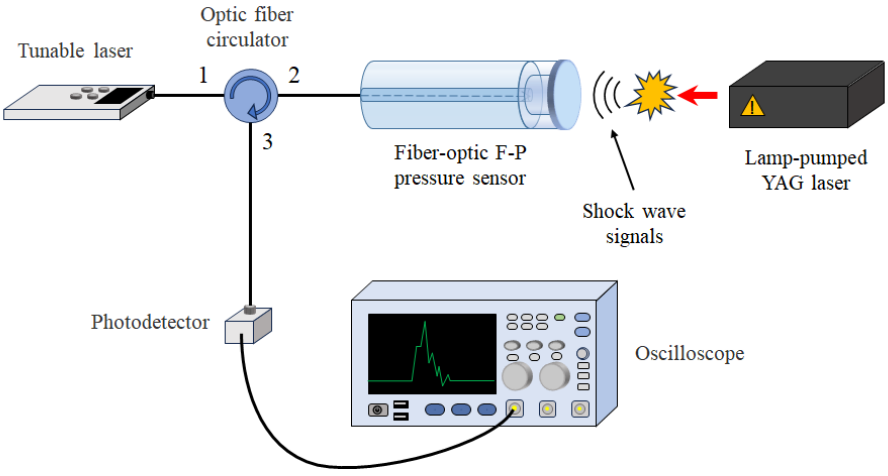

Fig. 14. Schematic diagram of dynamic pressure measurement experimental system (colour online)

As depicted in Fig. 15(a), the experimental system was designed such that light with a wavelength of 1563.1 nm, emitted from the tunable laser, passed through port 1 of the fiber optic circulator and reached the fiber-optic F-P pressure sensor at port 2.

During the explosion, the reflected light carrying the shock wave pressure signal was transmitted through port 3 of the circulator to the photodetector, where it was converted into an electrical signal and subsequently displayed and stored on the oscilloscope.

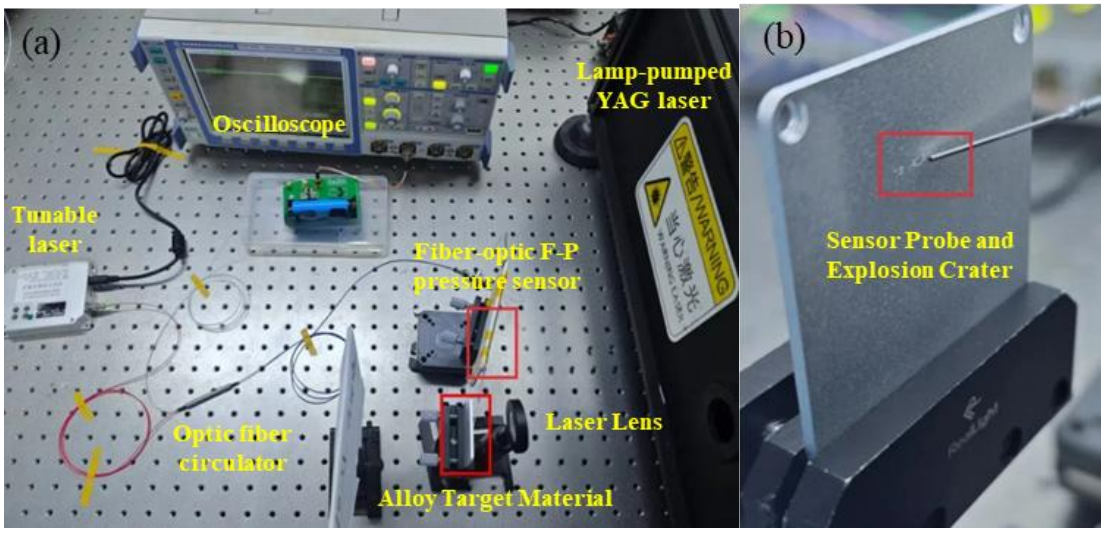

Fig. 15. (a) Experimental setup. (b) Sensor probe position (colour online)

During the experiment, the encapsulated sensor was fixed at the focal point of the laser lens, which corresponds to the explosion center, as shown in Fig. 15(b). A shock wave was produced by a lamp-pumped YAG laser. The sensor captured the shock wave pressure signal, which was subsequently displayed on the oscilloscope through the photodetector. The recorded shock wave signal is depicted in Fig. 16(a). The sensor was triggered at 1.639 μs, producing a shock wave signal on the oscilloscope that peaked at 1.753 μs. A rise time of 114 ns and a voltage change of 40.8 mV were observed in the recorded shock wave signal. It can be observed a 4.5 μs oscillation on the voltage signal. After reaching front surface of the FP sensor, the shockwave can continuously propagate in the FP cavity, and propagate back and forth in the FP cavity, which can result the short period oscillation of the FP cavity length and maybe the reason for the small oscillation overlapped on the waveform. Based on the sensor's voltage sensitivity of 9.86 mV/MPa, the voltage values were converted into pressure, and the resulting shock wave pressure curve is depicted in Fig. 16(b). During the dynamic pressure measurement experiment, the recorded dynamic signal displayed a pressure value of 4.02 MPa, consistent with the characteristics of the shock wave signal. This indicates that the sensor can effectively respond to shock wave signals produced by a lamp-pumped YAG laser and accurately measure shock wave pressure.

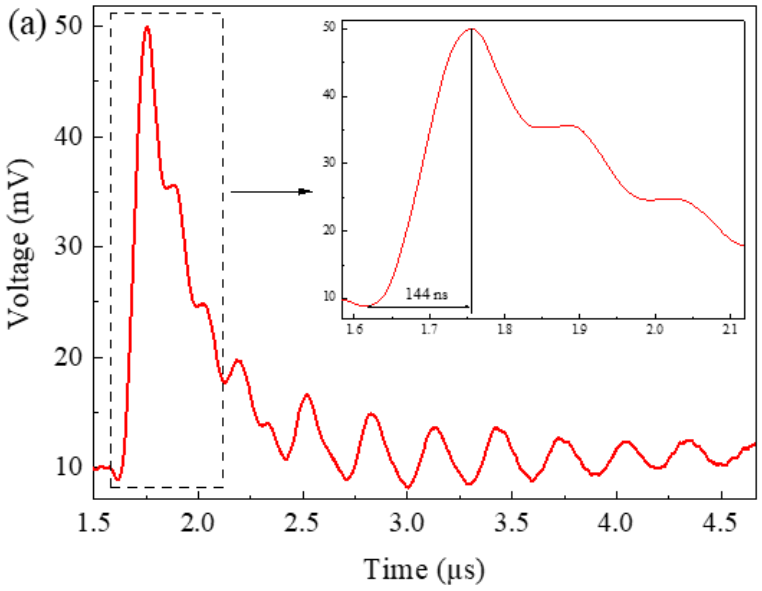

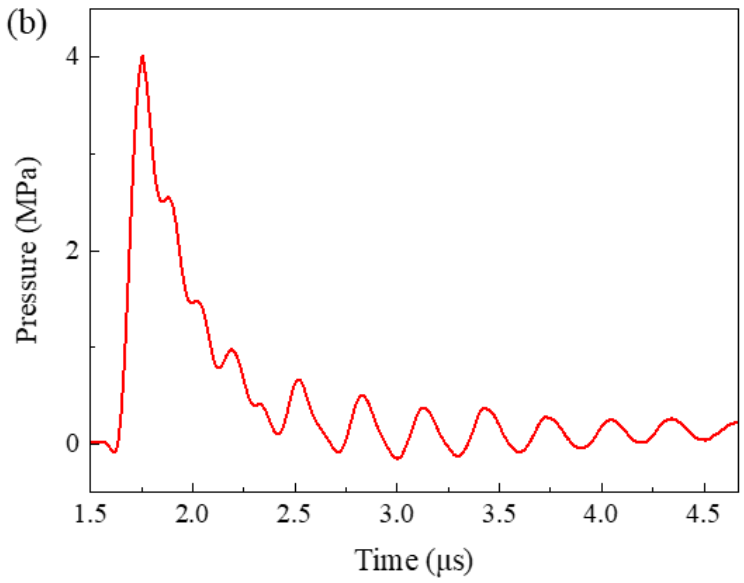

Fig. 16. (a) Voltage signal of shock wave. (b) Pressure signal of shock wave (colour online)

Table 1 presents the characteristics of different sensors. A highly sensitive fiber-optic F-P sensor based on the Vernier effect, utilizing parallel polymer air cavities, is introduced in Reference [27]. Although it demonstrates high sensitivity, its pressure range is limited to 0 ~ 2 MPa, and it is incapable of responding to dynamic pressure signals. Reference [28] proposes a suspended fiber-optic F-P sensor, a thin-cladding fiber (TCF) is inserted into a silica capillary wherein the end faces of the TCF and single-mode fiber form a suspended F-P structure. It is capable of static pressure measurements within a range of 0 ~ 80 MPa, but its sensitivity is only 2.97 nm/MPa, and it cannot perform dynamic pressure measurements. Reference [29] proposes an all-fiber F-P sensor capable of measuring dynamic pressure, with a static pressure sensitivity as high as 55.3 nm/MPa. However, its measurement range is limited to 0 ~ 16 MPa. Additionally, the diaphragm of this sensor is composed of coreless fiber, and the reflected light from the outer surface of the diaphragm cannot be eliminated through etching. In Reference [30], a fiber-optic dynamic pressure sensor based on a thin-film F-P cavity at the fiber end face is proposed. This sensor can measure dynamic pressure as well as static pressure within a range of 0 ~ 60 MPa, with a sensitivity of 0.32 nm/MPa. However, compared to the sensor presented in this work, its sensitivity is lower, and the fabrication cost is significantly higher due to the deposition of two gold layers on the end face.

Table 1. Comparison table

Sensor Type	Cavity length sensitivity (nm/MPa)	Pressure measurement range (MPa)	Dynamic pressure measurement	Ref.
Vernier effect F-P	36.9	0 ~ 2	No	[27]
Suspended F-P	2.97	0 ~ 80	No	[28]
All fiber F-P	55.3	0 ~ 16	Yes	[29]
Thin-film F-P cavity	0.32	0 ~ 60	Yes	[30]
All fiber F-P	5.14	0 ~ 60	Yes	This work

In summary, the sensor developed in this paper offers several advantages, including a wide static pressure measurement range, high sensitivity, simple fabrication, and low cost.

4. Conclusion

For wide-range high-pressure measurements, this study introduces an all-fiber F-P pressure sensor with an optimized SMF-HCF-MMF structure. Based on simulation analysis, the diaphragm thickness of the sensor was optimized to 14 μm. In static pressure measurements, the sensor exhibited a pressure range of

0~60 MPa, with a wavelength sensitivity of 96.4 pm/MPa, a cavity length sensitivity of 5.14 nm/MPa, and a voltage sensitivity of 9.86 mV/MPa. In dynamic pressure measurements, the sensor successfully captured a shock wave signal, exhibiting a pressure rise time of 114 ns and a pressure rise amplitude of 4.02 MPa. The sensor developed in this study demonstrates significant potential for high-pressure measurement applications. Nevertheless, the fabrication process yield currently remains below 100%. Future efforts will focus on utilizing more precise instruments and standardized fabrication protocols to enhance the yield. Furthermore, the sensor diaphragm will be refined through a combination of polishing and etching techniques to produce thinner pressure-sensitive diaphragms, thereby improving sensor performance.

Acknowledgements

This work is supported by the Open Fund of MCRI-Shannxi Laboratory of Energetic Materials No. WZKF2024105109.

References

[1] J. Yang, Sensors **13**(3), 2719 (2013).
[2] Y. Javed, M. Mohtashim, A. S. Irtiza, Sensor Review **39**(5), 652 (2019).
[3] Z. Shao, Yalin Wu, Shuang Wang, Yan Wang, Zhiqiang Sun, Wei Wang, Zhiyuan Liu, Bin Liu, Optics Express **30**(3), 3665 (2022).
[4] H. Kappert, S. Schopferer, N. Saeidi, R. Döring, S. Ziesche, A. Olowinsky, F. Naumann, M. Jägle, M. Spanier, A. Grabmaier, Conference on High Temperature Electronics Network (HiTEN 2022), July 18-20, 2022, St. Anne's College, Oxford, UK.
[5] Y. Deng, J. Jin, IEEE Sensors Journal **22**(14), 13811 (2022).
[6] S. Pevec, D. Denis, Optics Express **19**(16), 15641 (2011).
[7] Fei Feng, Pinggang Jia, Jiang Qian, Zhengpeng Hu, Guowen An, Li Qin, Micromachines **12**(623), 6 (2021).
[8] X. Wang, T. Chen, D. Meng, F. Wang, IEEE Sensors Journal **21**(1), 71 (2020).
[9] V. Geudens, Shahryar Nategha, Geert Van Steenberge, Jan Belis, Jeroen Missinne, Optics and Laser Technology **169**, 109970 (2024).
[10] Y. Ma, M. Zhao, J. Sun, C. Su, X. Li, Y. Li, Y. Yi, S. Wang, T. Geng, W. Sun, L. Yuan, IEEE Sensors Journal **21**(19), 21572 (2021).
[11] Li Zhao, Shuai Hao, Yunhao Chen, Enming Zhao, Chuanxi Xing, Jing Fan, Jianing Tang, Optics and Laser Technology **157**, 108670 (2023).
[12] Y. Wei, 22nd International Conference on Optical Communications and Networks (ICOCN), IEEE, 2024.
[13] T. Wei, X. Lan, H. Xiao, Y. Han, H.-L. Tsai, IEEE International Instrumentation and Measurement Technology Conference, IEEE, 2011.
[14] Y. Huang, T. Jin, G. Xu, Sensors **16**(9), 1424 (2016).
[15] Y. Du, B. Sun, J. Li, W. Zhang, Optical Fiber Sensing and Structural Health Monitoring Technology, Springer, Singapore, 31 (2019).
[16] Ye Chen, Dongqin Lu, Huan Xing, Haotian Ding, Junxian Luo, Hanwen Liu, Xiangxu Kong, Fei Xu, Sensors **24**(4), 1079 (2024).
[17] X. Hu, S. Dan, Q. Xueguang, Applied Optics **63**(10), 2658 (2024).
[18] Shubin Zhang, Zhenjun Shao, Jinrong Liu, Meixue Zong, Jian Shen, Haitao Gao, Guanjun Wang, Mengxing Huang, Coatings **10**(4), 358 (2020).
[19] Daniela Silva, Catarina S. Monteiro, Susana O. Silva, Orlando Frazão, Joana V. Pinto, Maria Raposo, Paulo A. Ribeiro, Susana Sério, Photonics **9**(5), 342 (2022).
[20] Yinan Zhang, Lei Yuan, Xinwei Lan, Amardeep Kaur, Jie Huang, Hai Xiao, Optics Letters **38**((22), 4609 (2013).
[21] Weiyi Ma, Yi Jiang, Jie Hu, Lan Jiang, Taojie Zhang, Taojie Zhang, Sensors and Actuators A: Physical **302**, 111795 (2020).
[22] Yingying Wang, Xiaohui Liu, Xiaoan Chen, Zhihui Sun, Qingchao Zhao, Journal of Wuhan University of Technology-Mater. Sci. Ed. **37**(6), 1143 (2022).
[23] Yuzhuo Miao, Feng Xue, Mingwei Li, Kun Ren, Ning Zhou, Hongxia Zhang, Gagong Jia, Haojun Fan, Optics Communications **573**, 131015 (2024).
[24] Chen Qin, Xiqing Guo, Jing Zhou, Chenxi Wang, Jingyu Rong, Qiang Zhang, Gang Li, Pengfei Zhang, Tiancai Zhang, Optics Express **32**(8), 14780 (2024).
[25] Vladimir Fedorov, Dmitry Martyshkin, Krishna Karki, Sergey Mirov, Optics Express **27**(10) 13934 (2019).
[26] B. Campanella, S. Legnaioli, S. Pagnotta, F. Poggialini, V. Palleschi, Atoms **7**(2), 57 (2019).
[27] R. Pan, W. Yang, L. Li, Y. Yang, L. Zhang, X. Yu, J. Fan, S. Yu, Y. Xiong, IEEE Sensors Journal **21**(19), 21577 (2021).
[28] G. Dai, S. Dan, X. Qiao, IEEE Transactions on Instrumentation and Measurement **71**, 1 (2022).
[29] C. Chu, J. Wang, J. Qiu, IEEE Sensors Journal **21**(12), 13296 (2021).
[30] X. Zhang, Z. Sun, X. Zhao, Z. Gao, Acta Optica Sinica **44**(7), 0728003 (2024).

*Corresponding author: xue_l_x@163.com